JACS
JOURNAL OF THE AMERICAN CHEMICAL SOCIETY
Article
pubs.acs.org/JACS

Electrocatalytically Active Graphene–Porphyrin MOF Composite for Oxygen Reduction Reaction

Maryam Jahan, Qiaoliang Bao, and Kian Ping Loh*

Graphene Research Centre, Department of Chemistry, National University of Singapore, 3 Science Drive 3, Singapore 117543

Supporting Information

ABSTRACT: Pyridine-functionalized graphene (reduced graphene oxide) can be used as a building block in the assembly of metal organic framework (MOF). By reacting the pyridine-functionalized graphene with iron–porphyrin, a graphene–metalloporphyrin MOF with enhanced catalytic activity for oxygen reduction reactions (ORR) is synthesized. The structure and electrochemical property of the hybrid MOF are investigated as a function of the weight percentage of the functionalized graphene added to the iron–porphyrin framework. The results show that the addition of pyridine-functionalized graphene changes the crystallization process of iron–porphyrin in the MOF, increases its porosity, and enhances the electrochemical charge transfer rate of iron–porphyrin. The graphene–metalloporphyrin hybrid shows facile 4-electron ORR and can be used as a promising Pt-free cathode in alkaline Direct Methanol Fuel Cell.

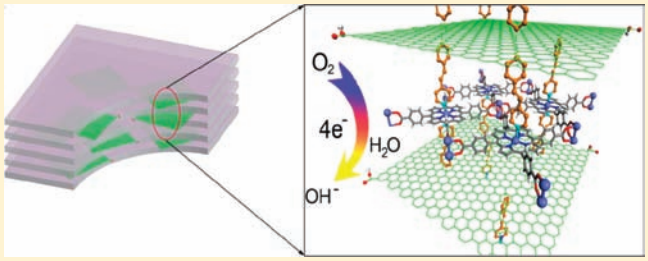

INTRODUCTION

Graphene, a two-dimensional sheet of sp^2 conjugated carbon atoms,[1] can be considered as a giant polyaromatic platform for performing chemistry due to its open ended structure.[2] The combination of high specific surface area (theoretical value of ~2600 m^2/g)[3,4] and high electrical conductivity[5,6] makes graphene sheets highly promising as an electrocatalyst platform.[7] Graphene oxide (GO) is the solution-dispersible form of graphene. The presence of epoxy and hydroxyl functional groups on either side of the GO sheet[8] impart bifunctional properties on the material[9] which allow it to act as structural nodes in metal organic framework (MOF).[10,11] One attractive approach to MOF-based catalyst design is to heterogenize known homogeneous molecular catalysts by employing them as struts, linking organometallic nodes. Indeed, some of the earliest reports on crystalline MOFs emphasized the potential of porphyrins as building blocks.[12]

Iron porphyrins play a vital role in oxygen transport and reduction reactions in biological systems.[13,14] Cathodic oxygen reduction reaction (ORR) is an active area of research because of its crucial role in electrochemical energy conversion in fuel cells.[15] Direct Methanol Fuel Cell (DMFC) is typically composed of three major components: a Pt–Ru anode for methanol oxidation,[16,17] a Pt cathode for oxygen reduction,[18] and a proton exchange membrane[19] (PEM). DMFC operates by oxidizing an aqueous solution of methanol to CO_2 and reducing oxygen to water. Usually the kinetics of the ORR is very slow and requires an efficient catalyst for the ORR cathode.[20] To date, the most efficient catalysts for ORR is platinum-based. The drawback is even at high Pt loading (0.4 mg/cm^2), the activation potential for ORR is on the order of 500 mV in acid. Large-scale commercialization is prohibited by the high cost of platinum.[20]

Compared to the acidic DMFCs, alkaline DMFCs have advantages such as more facile electrode catalytic reactions, lower methanol permeability from anode to cathode and simpler water management.[21] It is attractive to consider if iron phophyrin supported on graphene can function as an alternative to Pt-based electrode in fuel cells for ORR in alkaline media. In this work, we employed reduced GO (r-GO) sheets that are functionalized on either side of the basal plane with pyridine ligands; these function as struts to link metalloporphyrin nodes to form the hybrid graphene-MOF framework. At the same time, the oxygenated functional groups on r-GO can facilitate ORR by acting as an electron transfer mediator. We found that the presence of r-GO linked to pyridine ligands in MOF actually increases the electrocatalytic activity of the iron porphyrin and faciliate ORR via 4-electrons reaction. In addition, methanol crossover reaction is minimized by the inactivity of the hybrid MOF to methanol oxidation.

RESULTS AND DISCUSSION

The chemical structures of the various subunits in the assembled MOF are illustrated in Scheme 1. The porphyrin used in this structure is 5,10,15,20-tetrakis(4-carboxyl)-21*H*,23*H*-porphyrin, which is abbreviated as TCPP. The MOF is created by linking TCPP and $FeCl_3$, herewith abbreviated as $(Fe–P)_n$ MOF. G-dye represents r-GO sheets that are functionalized with donor-π-acceptor dye which terminates in pyridinium moieties (electron-withdrawing

Received: December 15, 2011
Published: March 22, 2012

   dx.doi.org/10.1021/ja211433h | *J. Am. Chem. Soc.* 2012, 134, 6707–6713

Scheme 1. Schematic of the Chemical Structures of (a) Reduced GO (r-GO), (b) G-dye, (c) TCPP, (d) $(Fe-P)_n$ MOF, (e) $(G\text{-dye-FeP})_n$ MOF, and (f) Magnified View of Layers Inside the Framework of $(G\text{-dye-FeP})_n$ MOF Showing How Graphene Sheets Intercalated between Prophyrin Networks[a]

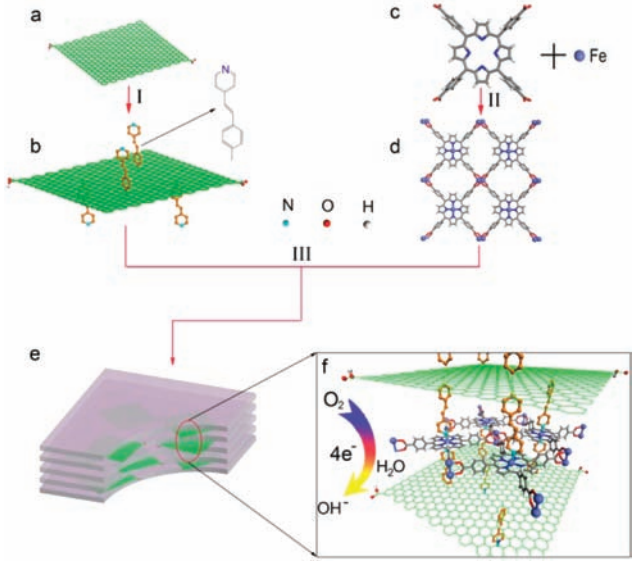

[a]Synthetic routes to make Graphene–Porphyrin MOF: (**I**) G-dye synthesized from r-GO sheets via diazotization with 4-(4-aminostyryl) pyridine, (**II**) $(Fe-P)_n$ MOF synthesized via reaction between TCPPs and Fe ions, (**III**) $(G\text{-dye-FeP})_n$ MOF formed via reaction between $(Fe-P)_n$ MOF and G-dye.

group). The pyridine ligand improves the solubility of the systems by stabilizing the electron-rich phenylethyl group, and prevents aggregation. The composite formed by the combination of G-dye and $(Fe-P)_n$ MOF is named as $(G\text{-dye-FeP})_n$ MOF. Previous work showed that the incorporation of nitrogen in carbon materials, especially in the form of the pyridinium moieties, is critical in enhancing the electrocatalytic activity for ORR.[22] This improved catalytic performance is ascribed to the electron accepting ability of the nitrogen atoms, which polarizes the adjacent carbon atom and enhances their bonding affinity with adsorbed OOH, thus, favoring the production of hydrogen peroxide, a product of the ORR.[23]

To study the structure–composition relationship, different weight percentages of G-dye (5, 10, 25, 50 wt %) were mixed with the chemical precursors of $(Fe-P)_n$ MOF to synthesize $(G\text{-dye 5, 10, 25, 50 wt \% -FeP})_n$ MOF composites. Because TCPP has a square planar symmetry decorated by carboxylic groups around the porphyrin site, it is perfectly suited for supramolecular assembly.[24] Sumod et al. reported the synthesis of 3D frameworks by dissolving of Mn (Cl)–TCPP in nitrobenzene under solvothermal condition.[25] Similarly, 3D MOF based on $(Fe-P)_n$ where P = porphyrin is synthesized by dissolving TCPP and $FeCl_3$. Graphene sheets decorated by pyridine groups on either side of the sheets are analogous to pillar connectors such as bpy, 4,4-bipyridine used in MOF synthesis.[26,27]

The first question is whether there are any differences in chemical structure between graphene–metalloporphyrin MOF and metalloporphyrin MOF without graphene. This is important to understand how graphene influences the crystallization of the MOF, and its properties and functionality. Therefore, we performed a systematic characterization of the optical absorption, vibrational bands and crystal structure of these composites to see if effects due to chemical hybridization, charge or energy transfer between the different components can be observed.

Figure 1a shows UV–vis absorption spectra of GO and G-dye in DMF. The absorption peak of GO[28] at 268 nm is due to

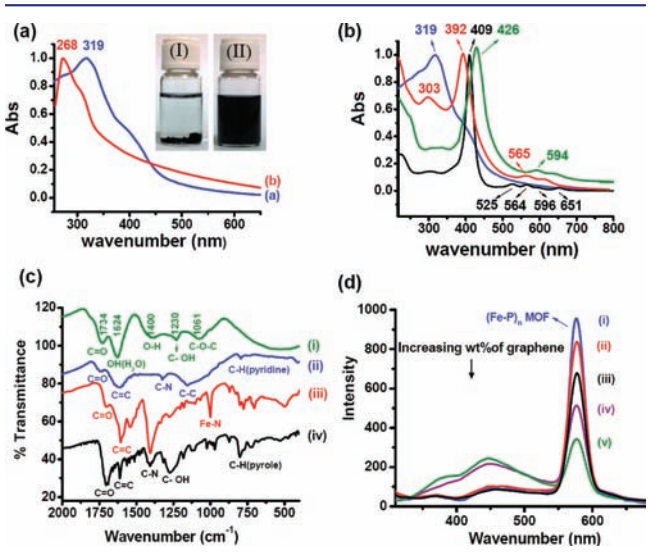

Figure 1. (a) UV–vis absorption spectra of (blue plot (a)) G-dye (3.7 mg L^{-1}) and (red plot (b)) GO (4.3 mg L^{-1}) in DMF. Inset image: comparison between solubility in DMF of r-GO (I) and G-dye (II). (b) black plot, UV–vis absorption spectra of TCPP (3.2 mg L^{-1}); red plot, $(G\text{-dye 10 wt \% -FeP})_n$ MOF (5.2 mg L^{-1}); green plot, $(Fe-P)_n$ MOF (4.9 mg L^{-1}); and blue plot, G-dye (4.7 mg L^{-1}) in phosphate buffer. (c) FTIR spectra of (i) GO, (ii) G-dye, (iii) $(G\text{-dye 10 wt \% -FeP})_n$ MOF, and (iv) TCPP. (d) Fluorescence spectroscopic changes observed for (i) $(Fe-P)_n$ MOF, (ii) $(G\text{-dye 5 wt \% -FeP})_n$ MOF, (iii) $(G\text{-dye 10 wt \% -FeP})_n$ MOF, (iv) $(G\text{-dye 25 wt \% -FeP})_n$ MOF, (v) $(G\text{-dye 50 wt \% -FeP})_n$ MOF (all concentrations are 2 mg L^{-1} in phosphate buffer solution). Excitation wavelength (426 nm).

the characteristic π-plasmon absorption.[29] The red-shifted $\pi-\pi^*$ absorption band at 319 nm of G-dye is consistent with the partial recovery of conjugated network[30] in r-GO and also a coupling effect of functional groups on the surface of graphene.[28] The absorption spectra of G-dye, TCPP, $(Fe-P)_n$ MOF and $(G\text{-dye 10 wt \% -FeP})_n$ MOF in phosphate buffer are shown in Figure 1b. The UV–vis spectrum of TCPP (black line) displays six characteristics bands, including an intense Soret band (409 nm) [deeper π levels $\rightarrow$ LUMO] and four characteristic visible absorption bands (Q-bands) at 525, 564, 596, and 651 nm [$\pi \rightarrow \pi^*$ electronic transition from the HOMO to the LUMO].[31] Coordination of the porphyrin with iron atoms to form iron porphyrinate (green line) results in a reduction of the Q bands from four to two in the UV–vis spectra and a red shift in the Soret band of $(Fe-P)_n$ MOF.[31] The presence of r-GO in $(G\text{-dye 10 wt \% -FeP})_n$ MOF (red line) creates a new band at 303 nm and a blue shift in Soret band compared to $(Fe-P)_n$ MOF (green line).

The functional groups present in the starting material and the different hybrids are characterized by fourier transform infrared spectroscopy (FTIR). As shown in Figure 1c(i), the vibrational peaks of GO are consistent with the presence of fingerprint groups such as carboxylic species, hydroxyl species and epoxy species (C=O, 1734 cm^{-1}; OH deformation, 1400

dx.doi.org/10.1021/ja211433h | J. Am. Chem. Soc. 2012, 134, 6707–6713

cm^{-1}; the C−OH stretching, 1230 cm^{-1}; C−O−C (epoxy group) stretching, 1061 cm^{-1}; skeletal ring stretch, 1624 cm^{-1}).[32] In the spectrum of G-dye (Figure 1c(ii)), the vibration of the C−O−C (epoxy group) is significantly reduced due to the fact that the skeletal framework in G-dye is made of reduced GO (r-GO). The functionalization of r-GO with the pyridine ligands gives rise to fingerprint bands which emerge at 798, 1150, 1331, 1605, and 1740 cm^{-1}, which can be assigned to C−H pyridine,[33] C−C bending,[34] C−N pyridine,[35] phenyl C═C ring stretch,[36] and C═O vibration of COOH,[37] respectively, in the G-dye. The spectrum of TCPP (Figure 1c(iv)) shows a triplet band at 1020, 985, and 966 cm^{-1} due to the well-resolved C−H rocking vibrations of the pyrrole ring.[38] The C═O stretching vibration in the COOH group in TCPP is seen at 1701 cm^{-1}; the bands in the range of 1500−1600 cm^{-1} are due to stretching vibration of C═C in the pyridyl aromatic ring.[39] The FTIR spectrum of (G-dye 10 wt % -FeP)$_n$ MOF (Figure 1c(iii)) largely resembles that of TCPP. A fingerprint band present at 1675 cm^{-1} is assigned to the C═O stretch of carboxylate group. The downshift of the C═O stretch from 170 to 1675 cm^{-1} as well as an intense fingerprint Fe−N stretching at 1008 cm^{-1} compared to that of TCPP reflects the metalation of porphyrin ring.[35,38]

Fluorescence spectra of the (Fe−P)$_n$ MOF and (G-dye-FeP)$_n$ MOF composites were recorded to examine the electronic interactions of G-dye sheets and Porphyrin-MOF units (Figure 1d). The observed luminescence quenching of the (Fe−P)$_n$ MOF, which has a strong fluorescence peak at 575.8 nm, reveals that there is a strong interaction between the excited state of TCPP and r-GO in the hybrid. The fluorescence quenching of the excited TCPP may be due to photoinduced electron transfer or energy transfer to the r-GO scaffold, which acts as a charge sink due to its conjugated network.[40]

Changes in the chemical environment of the iron and nitrogen in (Fe−P)$_n$ MOF and (G-dye 10 wt %-FeP)$_n$ MOF were also verified by X-ray photoelectron spectroscopy (Supporting Information, S8). According to CHN (carbon, hydrogen, and nitrogen content) elemental analysis, the amount of nitrogen in G-dye is between 7.1 and 9.8 wt %, which is evident of the sufficient amount of pyridine ligands for coordination-assisted assembly.

Powder X-ray diffraction was used to examine the phase and structure of the synthesized products, as shown in Figure S1. Increasing the content of G-dye in the composite from 5 to 50 wt % results in increased lattice distortion of MOF; therefore, gradual transformation of the crystalline MOF into the amorphous state is expected. G-dye plays the role of an impurity intercalant in the basic framework of (Fe−P)$_n$ MOF[10] (Table S1). Accompanying the change in crystal structure, the morphology of (Fe−P)$_n$ MOF crystal changes from plate shape to rod shape[27] when increasing amount of G-dye (5 and 10 wt %) is added, as shown in SEM images (Figure 2).

The adsorption surface area of the (G-dye-FeP)$_n$ MOF hybrids was evaluated using adsorption isotherm measurements. The adsorption of N_2 follows a type I isotherm with a Brunauer−Emmett−Teller surface area of 933 m^2/g (for (G-dye 50 wt % -FeP)$_n$ MOF). This compares favorably with zeolite[41,42] which has typical surface area in the range of 500 m^2/g, and is higher than that of porphyrin-based MOFs.[41,43,44] The important role of graphene in enhancing the adsorption surface area can be seen clearly from the scaling between the

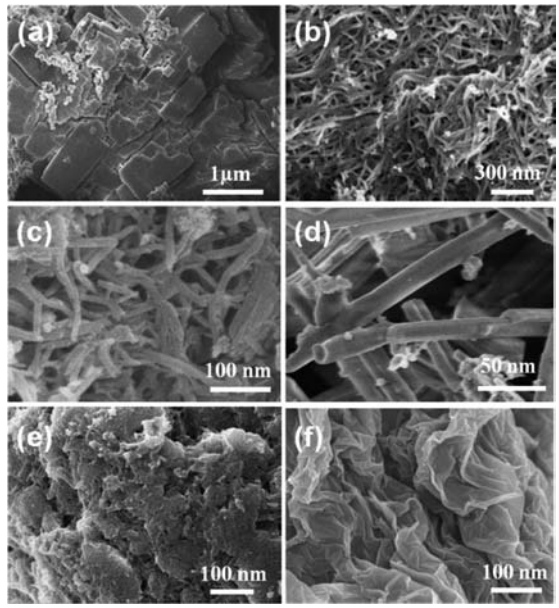

Figure 2. SEM images for (a) (Fe−P)$_n$ MOF, (b) (G-dye 5 wt % -FeP)$_n$ MOF, (c and d) (G-dye 10 wt %-FeP)$_n$ MOF, (e) (G-dye 25 wt % -FeP)$_n$ MOF, and (f) G-dye.

higher volume of adsorbed nitrogen ($cm^3\ g^{-1}$) with increasing amount of G-dye in the composite (Figure 3a).

The electrocatalytic activity of materials was examined by studying the redox reactions involving $Fe(CN)_6^{3-/4-}$ (Figure 3b) using cyclic voltammetry (CV). The effective surface area of the electrodes was estimated by cyclic voltammetry using 10 mM $Fe(CN)_6^{3-/4-}$ in 1 M KCl. The electroactive surface area can be estimated according to the Randles-Sevcik equation:[45,46]

$$i_p = 2.99 \times 10^5 nACD^{1/2}v^{1/2} \quad (1)$$

where i_p, n, A, C, D, and v are the peak current, the number of electrons involved in the reaction, the electroactive surface area, the concentration of the reactant, the diffusion coefficient of the reactant species, and the scan rate, respectively. The redox reaction of $Fe(CN)_6^{3-/4-}$ involves one-electron transfer (n = 1), and the diffusion coefficient (D) is 6.30×10^{-6} $cm^2\ s^{-1}$. The electroactive surface area of (G-dye 50 wt % -FeP)$_n$ MOF (10.98×10^{-2} cm^2) is nearly 20 times larger than that of bare GC electrode (0.55×10^{-2} cm^2). It is clear therefore that the incorporation of G-dye increases the electroactive surface area of the electrode and enhances the charge transfer kinetics.

The comparison between electrochemical activity of (G-dye 50 wt % -FeP)$_n$ MOF and GO is shown in Figure S2a. CV shows that the oxidation peak of GO is shifted to more negative potential compared to (G-dye 50 wt % -FeP)$_n$ MOF, which suggests that GO is a good catalyst for oxidation reaction. On the other hand, the reduction peak of (G-dye 50 wt % -FeP)$_n$ MOF is seen in more positive potential revealing facile reduction reaction for this catalyst compared to GO. The ΔE_p ($E_{pa} - E_{pc}$) values increase with increasing scan rate, but the formal potential ($E^{0\prime} = 1/2(E_{pc} + E_{pa})$) is almost constant, indicating the quasi-reversibility of the electron transfer process[47] (Figure S2b). The results in Figure 3b further demonstrate that the incorporation of G-dye can significantly increase the electrochemical activity of the electrode, as judged by nearly 10-fold increase in redox current with increasing

dx.doi.org/10.1021/ja211433h | J. Am. Chem. Soc. 2012, 134, 6707−6713

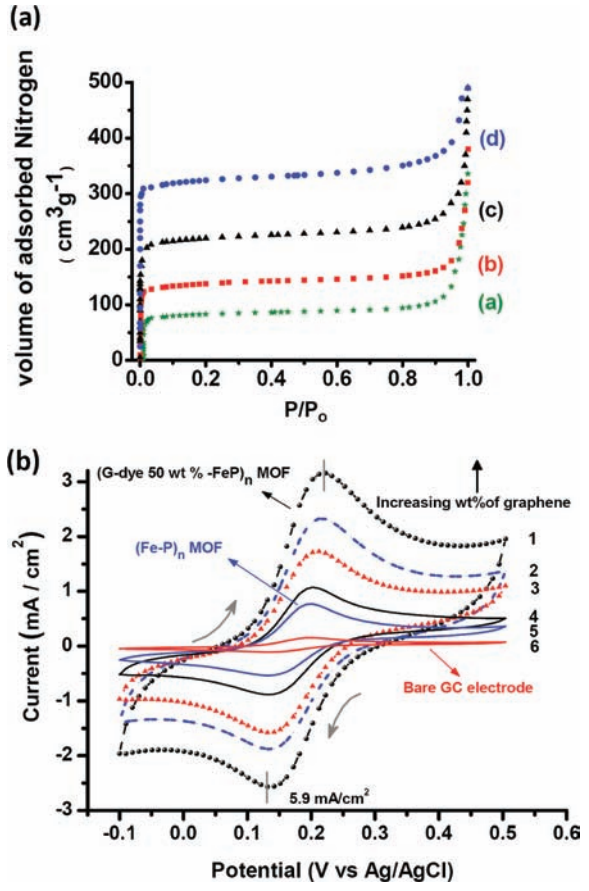

Figure 3. (a) Nitrogen gas sorption isotherms at 77 K for [green plot (a)] (G-dye 5 wt % -FeP)$_n$ MOF, [red plot (b)] (G-dye 10 wt % -FeP)$_n$ MOF, [black plot (c)] (G-dye 25 wt % -FeP)$_n$ MOF, and [blue plot (d)] (G-dye 50 wt % -FeP)$_n$ MOF. P/P_0 is the pressure (P) to saturation pressure (P_0) with P_0 = 746 Torr. (b) Cyclic voltammograms of 10 mM $Fe(CN)_6^{3-/4-}$ in 1 M KCl using different materials drop casted on GC electrode: (1) (G-dye 50 wt % -FeP)$_n$ MOF, (2) (G-dye 25 wt % -FeP)$_n$ MOF, (3) (G-dye 10 wt % -FeP)$_n$ MOF, (4) (G-dye 5 wt % -FeP)$_n$ MOF, (5) (Fe−P)$_n$ MOF, and (6) bare GC electrode. Scan rate is 50 mV/s.

addition of G-dye to (Fe−P)$_n$ MOF compared to bare GC electrode.

The electrocatalytic activity of (G-dye 50 wt %-FeP)$_n$ MOF for ORR was examined by cyclic voltammetry in 0.1 M KOH solution saturated with either nitrogen or oxygen. As shown in Figure S3a, featureless voltammetric currents within the potentials of −0.8 V to +0.3 V are observed for (G-dye 50 wt % -FeP)$_n$ MOF in N_2-saturated solution. In contrast, a well-defined cathodic peak centered at −0.23 V is observed in the CV as the electrolyte solution is saturated with O_2, which indicates its origin to ORR.

To assess the suitability of (G-dye 50 wt %-FeP)$_n$ MOF as an electrocatalyst for cathode ORR, the methanol crossover effect should be investigated. In DMFC, crossover of methanol from anode to cathode can result in the loss of equilibrium electrode potential and poisoning of catalyst when the methanol is oxidized.[48] Thus, a good electrocatalyst must be inert to methanol oxidation. In this regard, the electrocatalytic activity of (G-dye 50 wt % -FeP)$_n$ MOF for the electrooxidation of methanol is tested, and we used Pt-catalyst loaded GC electrode as an internal control. As shown in Figure S3a,b, a strong response is observed for the Pt catalyst in O_2-saturated 0.1 M KOH solution with 3 M methanol, whereas no obvious response for (G-dye 50 wt % -FeP)$_n$ MOF is detected under the same testing conditions. Therefore, we can conclude that (G-dye 50 wt % -FeP)$_n$ MOF exhibits a high selectivity for ORR with a strikingly good tolerance of methanol crossover effects.

To investigate the performance of catalyst for ORR, (Fe−P)$_n$ MOF and (G-dye 5,10,25, and 50 wt % -FeP)$_n$ MOF were drop-casted on glassy carbon electrode. In Figure 4a, the

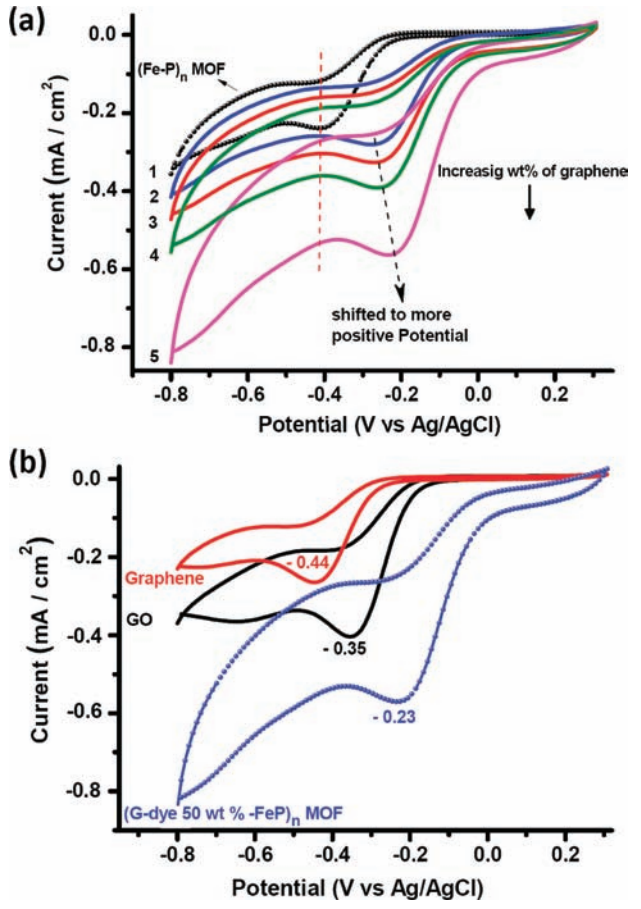

Figure 4. (a) Cyclic voltammograms of oxygen reduction on the (1) (Fe−P)$_n$ MOF, (2) (G-dye 5 wt % -FeP)$_n$ MOF, (3) (G-dye 10 wt % -FeP)$_n$ MOF, (4) (G-dye 25 wt % -FeP)$_n$ MOF, (5) (G-dye 50 wt % -FeP)$_n$ MOF electrodes obtained in O_2-saturated 0.1 M KOH at a scan rate of 50 mV/s. (b) Cyclic voltammograms of oxygen reduction on (1) exfoliated graphene, (2) GO, (3) (G-dye 50 wt % -FeP)$_n$ MOF electrodes in 0.1 M KOH O_2-saturated at a scan rate of 50 mV/s.

reduction potential for ORR is shifted increasingly to more positive values when the composition of G-dye increases in the MOF composite. The reduction by more than 200 mV in the oxygen reduction overpotential can be explained by the good electron transfer properties of the conductive G-dye sheets and increased electrochemical surface area in the sample. Figure 4b compared the performance of (G-dye 50 wt % -FeP)$_n$ MOF, GO and exfoliated graphite in ORR. It can be seen that GO is more electrocatalytically active compared to exfoliated graphite as judged from the positive shift of the overpotential for ORR by 90 mV and the increase in the current density. The enhanced kinetics for ORR in r-GO could be related to the presence of paramagnetic centers due to the formation of the aryloxy radical,[49] which enjoys resonance stabilization by the

dx.doi.org/10.1021/ja211433h | J. Am. Chem. Soc. 2012, 134, 6707−6713

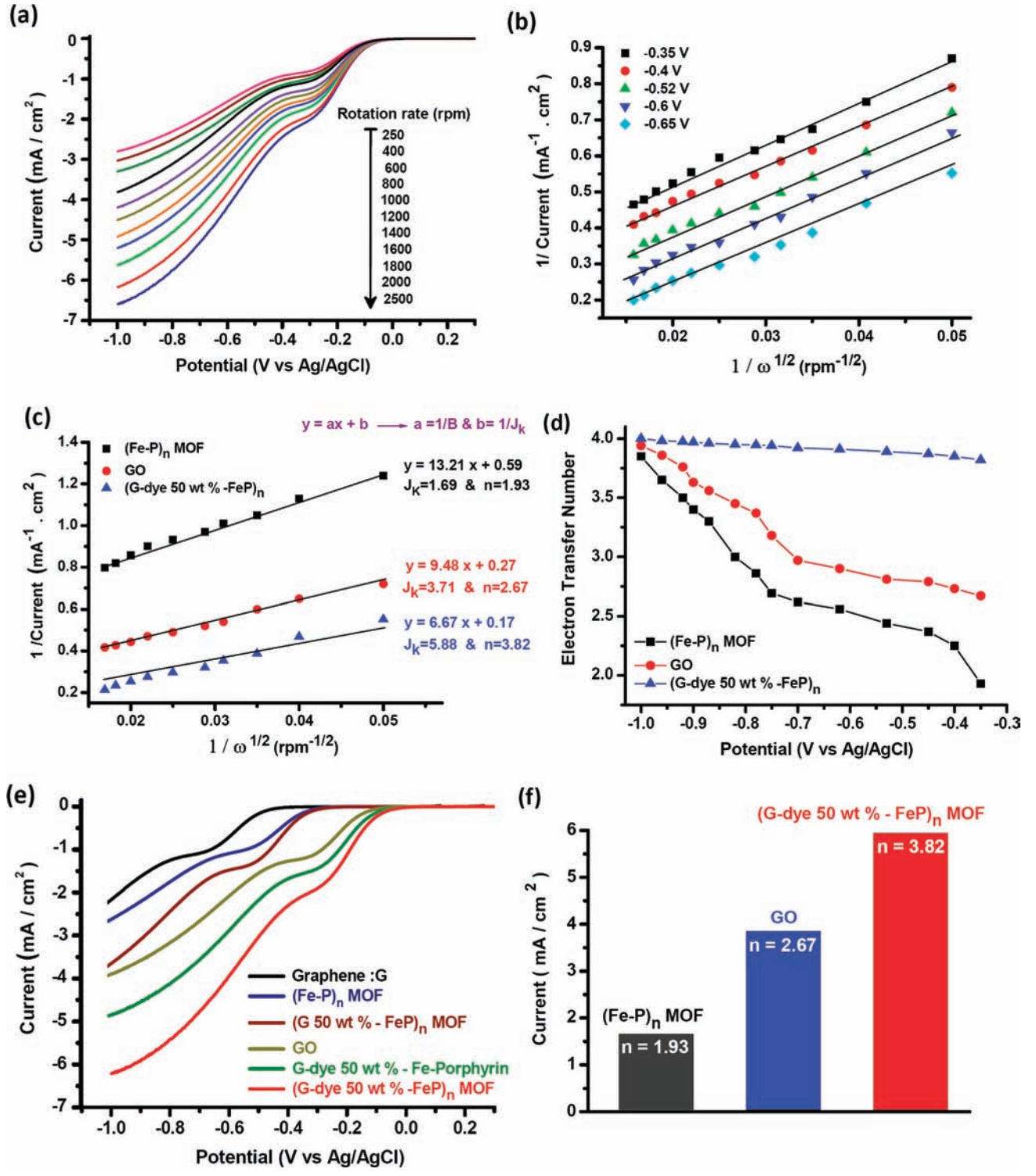

Figure 5. (a) Rotating disk electrode (RDE) linear sweep voltammograms of (G-dye 50 wt % -FeP)$_n$ MOF in O_2-saturated 0.1 M KOH with various rotation rates at a scan rate of 10 mV/s. (b) Koutecky–Levich plots at different electrode potentials of (G-dye 50 wt % -FeP)$_n$ MOF at different electrode potentials. (c) Koutecky–Levich plots of (G-dye 50 wt % -FeP)$_n$ MOF, (Fe–P)$_n$ MOF and GO at −0.65 V. (d) The dependence of the electron transfer number on the potential for (G-dye 50 wt % -FeP)$_n$ MOF, (Fe–P)$_n$ MOF and GO at various potentials. (e) RDE voltammograms of Graphene, (Fe–P)$_n$ MOF, (G 50 wt % -FeP)$_n$ MOF, G-dye 50 wt % -Fe-Porphyrin, (G-dye 50 wt % -FeP)$_n$ MOF and GO at a rotation rate of 2000 rpm. (f) Electrochemical activity given as the fully diffusion-limited current density (J_K) at −0.65 V for (Fe–P)$_n$ MOF, (G-dye 50 wt % -FeP)$_n$ MOF and GO.

aromatic scaffold in reduced GO. The charged surface state facilitates ORR by acting as an electron transfer mediator. Interestingly, the overpotential for ORR in (G-dye 50 wt % -FeP)$_n$ MOF-modified cathode is shifted positively by 120 mV compared to GO and the ORR current density of the composite is the highest among the three samples. These improvements in catalytic activities can be explained by the synergistic effects of framework porosity, a larger bond polarity

dx.doi.org/10.1021/ja211433h | J. Am. Chem. Soc. 2012, 134, 6707–6713

due to nitrogen ligand in the G-dye and the catalytically active iron−porphyrin in the structure of the hybrid MOF.

To obtain insight into the electron transfer kinetics of $(Fe-P)_n$ MOF, $(G\text{-dye 50 wt \% -FeP})_n$ and GO during the ORR, we studied the reaction kinetics by rotating-disk voltammetry. The voltammetric profiles in O_2-saturated 0.1 M KOH show that the current density is enhanced by an increase in the rotation rate from 250 to 2500 rpm (Figure 5a).

The corresponding Koutecky− Levich plots (J^{-1} vs $\omega^{-1/2}$) at various electrode potentials show good linearity (Figure 5b). Linearity and parallelism of the plots are considered as typical of first-order reaction kinetics with respect to the concentration of dissolved O_2. The kinetic parameters can be analyzed on the basis of the Koutecky− Levich equations:[50]

$$\frac{1}{J} = \frac{1}{J_L} + \frac{1}{J_K} = \frac{1}{B\omega^{1/2}} + \frac{1}{J_K} \quad (2)$$

$$B = 0.62nFC_0(D_0)^{2/3}\nu^{-1/6} \quad (3)$$

$$J_K = nFkC_0 \quad (4)$$

in which J is the measured current density, J_K and J_L are the kinetic and diffusion-limiting current densities, ω is the angular velocity of the disk ($\omega = 2\pi N$, N is the linear rotation speed), n is the overall number of electrons transferred in oxygen reduction, F is the Faraday constant ($F = 96485$ C mol^{-1}), C_0 is the bulk concentration of O_2, ν is the kinematic viscosity of the electrolyte, and k is the electrontransfer rate constant. As shown in Figure 5c, the number of electrons transferred (n) and J_K can be obtained from the slope and intercept of the Koutecky−Levich plots, respectively, and by using parameters $C_0 = 1.2 \times 10^{-3}$ mol L^{-1}, $D_0 = 1.9 \times 10^{-5}$ cm s^{-1}, and $\nu = 0.1$ m^2 s^{-1} in 0.1 M KOH.

ORR occurs either via the direct 4-electron reduction pathway where O_2 is reduced to H_2O or the 2-electron reduction pathway where it is reduced to hydrogen peroxide (H_2O_2). In fuel cell processes, the 4-electron direct pathway is preferred.

Figure 5d shows that in the case of cathodes using $(Fe-P)_n$ MOF or GO, the electron transfer number for ORR varies between 2 to 4 and is dependent on the overpotential, whereas the electron transfer number at the $(G\text{-dye 50 wt \% -FeP})_n$ MOF electrode is always ∼4, independent of the potential tested. The facile 4-electron transfer at a wide range of potential is consistent with the higher ORR current density observed for the cathode modified with $(G\text{-dye 50 wt \% -FeP})_n$ MOF and attests to the greater electrocatalytic capability of the hybrids where r-GO, pyrdinium linker and porphyrin catalyst act in concert in the charge transfer and electrochemical reduction processes.

To gain further insight into the structure−property correlation of $(G\text{-dye 50 wt \% -FeP})_n$ MOF composite during the ORR electrochemical process, we compared its electrocatalytic performance with (i) unfunctionalized graphene; (ii) $(Fe-P)_n$ MOF; (iii) $(G\ 50\ wt\ \%\ -FeP)_n$ MOF, which is a composite between unfunctionalised graphene and $(Fe-P)_n$ MOF and (iv) (G-dye 50 wt %)-$(Fe-P)_n$, which is a composite between G-dye (50 wt %) and $(Fe-P)_n$, using linear sweep voltammetry in an aqueous solution of O_2-saturated 0.1 M KOH (Figure 5e). The same amount of catalyst (159.2 μg·cm^{-2}) was loaded onto a GC rotating-disk electrode (RDE) each time. It was observed that the onset potential for ORR is the first to be reached in the $(G\text{-dye 50 wt \% -FeP})_n$ MOF and the oxygen reduction current densities of this electrode, at −6.2 mA·cm^{-2}, are higher than the rest. This suggests that the incorporation of G-dye into the MOF, as opposed to physical mixing of G-dye and MOF, offers better electrocatalytical behavior, due possibly to the unique structure of the hybrid where G-dye interconnects with the Fe-MOF in a 3-D manner.

The durability of $(G\text{-dye 50 wt \% -FeP})_n$ MOF as ORR catalyst for cathode was evaluated against Pt nanoparticles-loaded glassy carbon electrode and Ni foam. The test was performed using chronoamperometry at a constant voltage of −0.23 V in 0.1 M KOH solution saturated with O_2 (Figure S6). The corresponding current−time chronoamperometric response of $(G\text{-dye 50 wt \% -FeP})_n$ MOF exhibits a very slow attenuation after a 39% loss in its initial current density. In contrast, the Pt nanoparticles and Ni foam cathode show a current loss of approximately 58% and 52%, respectively. This result suggests that the durability of $(G\text{-dye 50 wt \% -FeP})_n$ MOF is superior to that of the Pt and Ni catalysts.

The graphene-MOF composite synthesized shows similar redox behavior in ORR when compared with previously reported Fe- and Co-phthalocyanines/multiwalled carbon nanotube (MWCNT) composite catalysts in alkaline media.[51] The FePc/MWCNTs composite has been found to be more active than Co composites for ORR with current density as high as −4.5 mA.cm^{-2} (at 1200 rpm, 185.2 μg/cm^2 catalyst loading) and onset ORR potential at −0.094 V versus SCE (saturated calomel electrode). The graphene-MOF hybrid catalyst exhibits similar current density as the FePc/MWCNTs composite but require lower sample (159.2 μg/cm^2) loading and exhibits a more positive ORR onset potential at −0.087 V vs SCE.

■ CONCLUSIONS

In summary, we have synthesized a hybrid MOF by adding pyridinium dye-functionalized r-GO sheets to the metalloporphyrin MOF. Our work points to the use of bifunctionalized r-GO as building blocks in MOF synthesis and as structural reinforcement filler which can extend and enhance the functionalities of MOF. Our studies reveal that functionalized r-GO sheets can influence the crystallization process of MOF and enhance the electrocatalytic properties of the composite when an appropriate amount is added. The presence of r-GO and pyridinium linker act synergistically with the porphyrin catalysts to afford facile 4-electron ORR pathway which is useful for DMFC operation. The composite also possesses a much higher selectivity for ORR and a significantly reduced methanol crossover effects compared to Pt catalyst.

■ ASSOCIATED CONTENT

Ⓢ Supporting Information

Experimental details, crystal and refinement data, cyclic voltammograms, stability and reproducibility of GO electrode, comparison of durability, X-ray photoelectron spectroscopy, UV absorption, TGA and DTA data, and more characterization data showing graphene in MOF. This material is available free of charge via the Internet at http://pubs.acs.org.

■ AUTHOR INFORMATION

Corresponding Author

chmlohkp@nus.edu.sg

Notes

The authors declare no competing financial interest.

■ ACKNOWLEDGMENTS

K.P.L. acknowledges the funding support of NRF-CRP grant "Graphene Related Materials and Devices" R-143-000-360-281. Q.B. acknowledges financial support from the LKY Postdoctoral Fellowship.

■ REFERENCES

(1) Rao, C.; Sood, A.; Subrahmanyam, K.; Govindaraj, A. *Angew. Chem., Int. Ed.* **2009**, *48*, 7752.
(2) Loh, K. P.; Bao, Q. L.; Ang, P. K.; Yang, J. X. *J. Mater. Chem.* **2010**, *20*, 2277.
(3) Si, Y.; Samulski, E. *Chem. Mater.* **2008**, *20*, 6792.
(4) Lightcap, I.; Kosel, T.; Kamat, P. *Nano Lett.* **2010**, *10*, 577.
(5) Geim, A.; Novoselov, K. *Nat. Mater.* **2007**, *6*, 183.
(6) Wang, X.; Zhi, L.; Mullen, K. *Nano Lett.* **2008**, *8*, 323.
(7) Bong, S.; Kim, Y.; Kim, I.; Woo, S.; Uhm, S.; Lee, J.; Kim, H. *Electrochem. Commun.* **2010**, *12*, 129.
(8) Dreyer, D.; Park, S.; Bielawski, C.; Ruoff, R. *Chem. Soc. Rev.* **2010**, *39*, 228.
(9) Lomeda, J.; Doyle, C.; Kosynkin, D.; Hwang, W.; Tour, J. *J. Am. Chem. Soc.* **2008**, *130*, 16201.
(10) Jahan, M.; Bao, Q. L.; Yang, J. X.; Loh, K. P. *J. Am. Chem. Soc.* **2010**, *132*, 14487.
(11) Petit, C.; Bandosz, T. J. *Adv. Mater.* **2009**, *21*, 4753.
(12) Shultz, A.; Farha, O.; Hupp, J.; Nguyen, S. *J. Am. Chem. Soc.* **2009**, *131*, 4204.
(13) Kodadek, T.; Raybuck, S. A.; Collman, J. P.; Brauman, J. I.; Papazian, L. M. *J. Am. Chem. Soc.* **1985**, *107*, 4343.
(14) Collman, J. P.; Brauman, J. I.; Suslick, K. S. *J. Am. Chem. Soc.* **1975**, *97*, 7185.
(15) Bashyam, R.; Zelenay, P. *Nature* **2006**, *443*, 63.
(16) Choi, J. H.; Park, K. W.; Kwon, B. K.; Sung, Y. E. *J. Electrochem. Soc.* **2003**, *150*, A973.
(17) Steigerwalt, E. S.; Deluga, G. A.; Cliffel, D. E.; Lukehart, C. *J. Phys. Chem. B* **2001**, *105*, 8097.
(18) Neergat, M.; Shukla, A.; Gandhi, K. *J. Appl. Electrochem.* **2001**, *31*, 373.
(19) Fernández, J. L.; Raghuveer, V.; Manthiram, A.; Bard, A. J. *J. Am. Chem. Soc.* **2005**, *127*, 13100.
(20) Jaouen, F.; Herranz, J.; Lefèvre, M.; Dodelet, J. P.; Kramm, U. I.; Herrmann, I.; Bogdanoff, P.; Maruyama, J.; Nagaoka, T.; Garsuch, A. *ACS Appl. Mater. Interfaces* **2009**, *1*, 1623.
(21) Xiong, Y.; Liu, Q. L.; Zhu, A. M.; Huang, S. M.; Zeng, Q. H. *J. Power Sources* **2009**, *186*, 328.
(22) Chen, Z.; Higgins, D. *Carbon* **2010**, *48*, 3057.
(23) Sidik, R. A.; Anderson, A. B.; Subramanian, N. P.; Kumaraguru, S. P.; Popov, B. N. *J. Phys. Chem. B* **2006**, *110*, 1787.
(24) Lipstman, S.; Muniappan, S.; George, S.; Goldberg, I. *Dalton Trans.* **2007**, 3273.
(25) George, S.; Lipstman, S.; Muniappan, S.; Goldberg, I. *CrystEngComm* **2006**, *8*, 417.
(26) Choi, E.; Barron, P.; Novotny, R.; Son, H.; Hu, C.; Choe, W. *Inorg. Chem.* **2008**, *48*, 426.
(27) Chung, H.; Barron, P. M.; Novotny, R. W.; Son, H. T.; Hu, C.; Choe, W. *Cryst. Growth Des.* **2009**, *9*, 3327.
(28) Wu, J.; Shen, X.; Jiang, L.; Wang, K.; Chen, K. *Appl. Surf. Sci.* **2010**, *256*, 2826.
(29) Rance, G. A.; Marsh, D. H.; Nicholas, R. J.; Khlobystov, A. N. *Chem. Phys. Lett.* **2010**, *493*, 19.
(30) Zhou, Y.; Bao, Q. L.; Tang, L. A. L.; Zhong, Y. L.; Loh, K. P. *Chem. Mater.* **2009**, *21*, 2950.
(31) Zhou, W.; Hu, B.; Liu, Z. *Appl. Catal., A* **2009**, *358*, 136.
(32) Xu, Y.; Bai, H.; Lu, G.; Li, C.; Shi, G. *J. Am. Chem. Soc.* **2008**, *130*, 5856.
(33) Cunliffe-Jones, D. *Spectrochim. Acta* **1965**, *21*, 747.
(34) Chen, A.; Yang, D.; Lipkowski, J.; Sun, S.; Pettinger, B. *Can. J. Chem.* **1996**, *74*, 2321.
(35) Yuan, Y.; Ji, H.; Chen, Y.; Han, Y.; Song, X.; She, Y.; Zhong, R. *Org. Process Res. Dev.* **2004**, *8*, 418.
(36) Sun, X.; Liu, Z.; Welsher, K.; Robinson, J.; Goodwin, A.; Zaric, S.; Dai, H. *Nano Res.* **2008**, *1*, 203.
(37) Wang, H.; Hao, Q.; Yang, X.; Lu, L.; Wang, X. *Electrochem. Commun.* **2009**, *11*, 1158.
(38) Sato, T.; Mori, W.; Kato, C.; Yanaoka, E.; Kuribayashi, T.; Ohtera, R.; Shiraishi, Y. *J. Catal.* **2005**, *232*, 186.
(39) Fagadar-Cosma, E.; Enache, C.; Armeanu, I.; Fagadar-Cosma, G. *Dig. J. Nanomater. Biostruct.* **2007**, *2*, 175.
(40) Liu, Z. B.; Xu, Y. F.; Zhang, X. Y.; Zhang, X. L.; Chen, Y. S.; Tian, J. G. *J. Phys. Chem. B* **2009**, *113*, 9681.
(41) Smithenry, D. W.; Wilson, S. R.; Suslick, K. S. *Inorg. Chem.* **2003**, *42*, 7719.
(42) Suslick, K. S.; Bhyrappa, P.; Chou, J. H.; Kosal, M. E.; Nakagaki, S.; Smithenry, D. W.; Wilson, S. R. *Acc. Chem. Res.* **2005**, *38*, 283.
(43) Ma, B. Q.; Mulfort, K. L.; Hupp, J. T. *Inorg. Chem.* **2005**, *44*, 4912.
(44) Ohmura, T.; Usuki, A.; Fukumori, K.; Ohta, T.; Ito, M.; Tatsumi, K. *Inorg. Chem.* **2006**, *45*, 7988.
(45) Guo, C.; Hu, F.; Li, C. M.; Shen, P. K. *Biosens. Bioelectron.* **2008**, *24*, 819.
(46) Guo, C. X.; Lei, Y.; Li, C. M. *Electroanalysis* **2011**, *23*, 885.
(47) Zhang, G.; Yang, F. *Electrochim. Acta* **2007**, *52*, 6595.
(48) Jiang, R.; Chu, D. *J. Electrochem. Soc.* **2004**, *151*, A69.
(49) Paliteiro, C.; Hamnett, A.; Goodenough, J. B. *J. Electroanal. Chem.* **1987**, *233*, 147.
(50) Liu, R.; Wu, D.; Feng, X.; Müllen, K. *Angew. Chem., Int. Ed.* **2010**, *122*, 2619.
(51) Morozan, A.; Campidelli, S.; Filoramo, A.; Jousselme, B.; Palacin, S. *Carbon* **2011**, *49*, 4839.